Refinable bi-quartics for design and analysis

Kęstutis Karčiauskas[a] and Jörg Peters[b]
[a] Naugarduko 24, Vilnius University, LT-2006, Vilnius, Lithuania
[b] Dept CISE, University of Florida, Gainesville FL 32611-6120, USA, jorg@cise.ufl.edu, tel/fax 352.392.1200/1220

Abstract

To be directly useful both for shape design and a thin shell analysis, a surface representation has to satisfy three properties: (1) be compatible with CAD surface representations, (2) yield generically a good highlight distribution, and (3) offer a refinable space of functions on the surface. Here we propose a new construction, based on a number of recently-developed techniques, that satisfies all three criteria. The construction converts quad meshes with irregularities, where more or fewer than four quads meet, to C^1 (or, at the cost of more pieces, C^2) bi-4 surface consisting of subdivision rings for the main body completed by a tiny G^1 cap.

1. Introduction

Modern piecewise polynomial constructions are based on careful parameterizations to achieve generically good highlight line distributions also where more or fewer than four 4-sided pieces meet. This representation is directly compatible with current CAD surface standards. Remarkably, such G^k constructions automatically provide a C^k space of functions on the surfaces [1, 2]. However, nested refinement of the G^k representation requires careful tracking of the original G^k edges to ensure that a solution obtained at one level of refinement is not lost at the next finer one. Already when $k = 1$, the characterization of all possible degrees of freedom, even when joining just one pair of patches, is not easy [3]. For specific high-end surface constructions, where the degrees of freedom under refinement have been explicitly characterized, they are heterogeneously distributed [4].

An alternative is to model multi-sided surface pieces with an infinite sequence of nested polynomial surface rings so that nested refinement is built-in. Such generalized subdivision is exemplified by Catmull-Clark (CC) subdivision [5]. Unfortunately many parts of the CAD pipeline are not set up for infinite recursive definition. More importantly, as Fig. 1 illustrates, CC subdivision produces poor highlight lines even for simple configurations, such as joining two crossing pipes. Note the characteristic 'pinching' of highlight lines near the 6-valent irregularity.

Retaining the best of subdivision and geometrically continuous surface constructions leads to the approach of this paper. The key observation is that in practice, analysis works with a maximal anticipated refinement level ℓ for a given geometric design. We therefore propose to model multi-sided surface pieces as a sequence of C^1 surface rings closed off by an n-sided G^1-cap at the final anticipated refinement level.

a. Since the final surface consists of a fixed number of $3n\ell + 4n$ bi-4 (bi-quartic) surface pieces, it is CAD representable.
b. Since the surface rings and final cap carefully follow a guiding shape, good highlight line distribution as in Fig. 1 is observed without exception for an obstacle course of challenging configurations.
c. Since the maximal refinement level at the irregularity is realized by the G^1-cap, it need not be refined. And since the sequence of surface rings forms a C^1 complex, nested refinability amounts to standard regular spline refinement.

While non-trivial in its derivation, the bi-4 surface is efficiently constructed via pre-tabulated operators, akin to the more lightweight subdivision stencils of CC subdivision. The number of surface rings can be varied to suit the application.

Structure of the paper. Section 2 explains the input and basic tools used for the constructions: the corner jet constructor, maps of total degree and characteristic parameterizations. Section 3 describes the guide and Section 4 a guided subdivision. Section 6 characterizes the eigenstructure of this subdivision and reveals how it is inherited from a guide surface. Section 5 reformulates the bi-4 guided subdivision to look more like traditional CC subdivision. Section 7 sketches how G^1 caps yield a high-quality, hybrid construction with finitely many patches. Section 8 illustrates the surface quality according to alternatives and trade-offs that lead to the preferred bi-4 construction presented here.

2. Definitions and Setup

This section characterizes the input, operators, C^1 polynomial caps of total degree, and the reparameterizations used to define first the guide and then the final surface.

2.1. A B-spline-like control net for irregular layout

We consider as input a network of quadrilateral facets, short quads. Nodes where four quads meet are regular, otherwise *irregular*. We assume that each irregular node is surrounded by

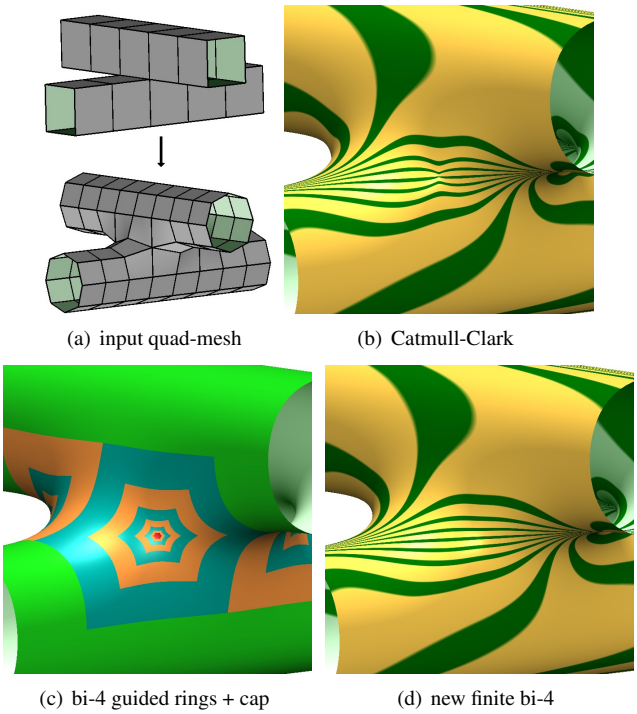

(a) input quad-mesh (b) Catmull-Clark

(c) bi-4 guided rings + cap (d) new finite bi-4

Figure 1: (a) Input mesh with (*top*) adjacent nodes of valence 6 and (*bottom*) once refined. (b) Pinched highlight lines typical of Catmull-Clark subdivision surfaces. (c) regular surface of degree bi-3 (green) and C^1 bi-4 guided rings with tiny G^1 bi-4 cap (red) covering the 6-sided region with a guided surface with (d) good highlight line distribution.

at least one layer of regular nodes. Fig. 2a shows the $\mathbf{c}$-net (bullets) of an isolated node of valence $n = 5$. The $\mathbf{c}$-net consists of the irregular node plus $6n$ nodes forming two layers of quads surrounding it. Typically a third layer is added for evaluation of local shape. The extra layer provides a surrounding surface (green in Fig. 2b). This allows tracing the highlight line distribution [6] across the transition where quality is as important and challenging as the internal quality of the cap.

Each 4×4 sub-grid of nodes is interpreted as the B-spline control points of a bicubic tensor-product spline surface. Except at the irregular node, well-known formulas can be applied to convert the B-spline form to Bernstein-Bézier form (see e.g. [7, 8]). The tensor-product Bernstein-Bézier (BB) form of bi-degree d is

$$\mathbf{p}(u,v) := \sum_{i=0}^{d}\sum_{j=0}^{d} \mathbf{p}_{ij} B_i^d(u) B_j^d(v) \,,$$

$$(u,v) \in \square := [0..1]^2, \qquad \text{where } B_k^d(t) := \binom{d}{k}(1-t)^{d-k}t^k$$

are the BB-polynomials of degree d and $\mathbf{p}_{ij}$ are the BB coefficients. Fig. 2b also shows the C^2 prolongation of this surface ring, i.e. Hermite data represented as a grid (black) of bi-3 BB-coefficients. Specifically, the BB-coefficients $\mathbf{p}_{ij}$, $i = 0, \ldots, 3$, $j = 0, \ldots, 2$, represent Hermite data of order 2 along one boundary curve $v = 0$. Degree-raised to bi-degree 4, we call these data $\mathbf{t}_{CC}$. In the remainder of this paper, we refer to

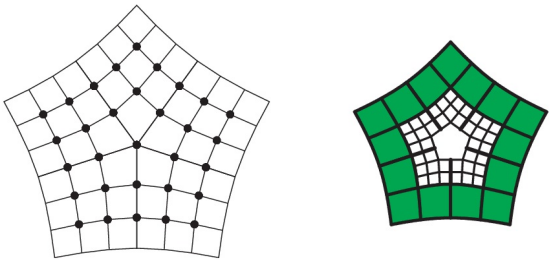

(a) $\mathbf{c}$-net extended by 1 layer (b) bi-3 ring + tensor-border

Figure 2: B-spline-like irregular control net and tensor-border. (a) Extended $\mathbf{c}$-net for $n = 5$. (b) Schema of surface ring (green) and its tensor-border (of degree 3 and depth 2 = inner grid of BB-coefficients). The tensor-border is the input for the multi-sided construction.

second-order Hermite data of degree 4 along the loop of boundary curves as one of

$$\mathbf{t}, \mathbf{h} = \text{a tensor-border of degree } 4 \text{ and depth } 2.$$

We will construct tensor-product patches and tensor-borders with the help of jet constructors

$$[f]^d_{i\times j}, \qquad \text{the corner jet constructor,}$$

expresses, at a corner of the domain square $[0..1]^2$, the expansion of a function f of order $i-1$ in u and $j-1$ in v in BB-form of bi-degree d. That is, $[f]^d_{i\times j}$ outputs $i \times j$ BB-coefficients (see Fig. 3a,b for $i = 3 = j$). Fig. 3c displays four corner jet constructors $[f]^4_{3\times 3}$ merged to form a bi-4 patch by averaging the overlapping BB-coefficients.

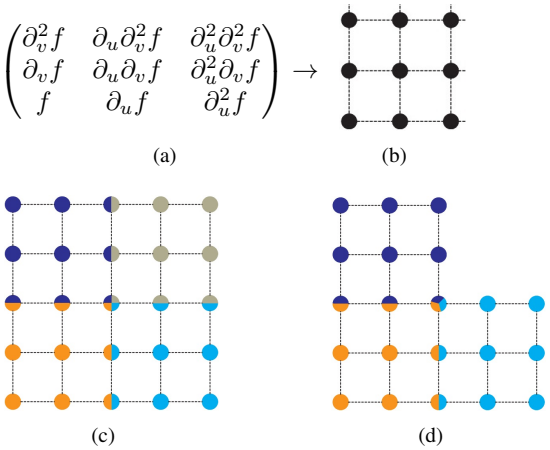

(a) (b) (c) (d)

Figure 3: Corner jet constructor $[f]^d_{3\times 3}$ at work. (a) Hermite data as partial derivatives converted to (b) BB-form assembled, by averaging 3×3 jets, into (c) a patch of degree bi-4. (d) L-shaped sector of the tensor-border $\mathbf{t}$.

Fig. 3d illustrates the analogous assembly of an L-shaped sector of the tensor-border by applying and averaging a jet constructor at three corners.

Several steps of the surface construction use a simple symmetric rule, called C2-rule in the following and illustrated in Fig. 4: two curve segments (of the same degree) in BB-form

join C^2 at their common end-point (marked as a big bullet) if and only if the BB-coefficient immediately to its *left* (small circle indicated by $\downarrow$ in Fig. 4) is defined as the weighted average of the BB-coefficients marked as bullets with the weights indicated above. The *right* circled BB-coefficient is defined by the mirrored formula.

Figure 4: Symmetric rule of C^2 join.

2.2. *Maps of total degree d*

We will use maps $\mathbf{b}^{\triangle}$ of total degree d whose domain is a regular n-gon D composed from n equal triangles with a common vertex $\mathbf{O}$ at the origin. Fig. 5a shows one such triangle with sides defined by $l_i = 0$, $i = 0, 1, 2$. Each linear function l_i is equal to 1 at the vertex opposite to $l_i = 0$. On the triangle we define a map $\mathbf{b}$ of *total degree* d in Bernstein-Bézier form as

$$\mathbf{b} := \sum_{i+j+k=d} \mathbf{b}_{ijk} B^d_{ijk}, \;\; i,j,k \geq 0, \qquad B^d_{ijk} := \binom{d}{ijk} l_0^i l_1^j l_2^k \,. \tag{1}$$

Fig. 5b labels the BB-coefficients rotationally symmetric. Let $\mathsf{c} := \cos \frac{2\pi}{n}$. Pieces on adjacent sectors $\mathbf{b}^s$ and $\mathbf{b}^{s+1}$ join

$$C^0 \text{ if } \quad \mathbf{b}^{s+1}_{d-i,i,0} := \mathbf{b}^s_{d-i,0,i}, \quad i=0,\ldots,d \tag{2}$$

$$C^1 \text{ if } \quad \mathbf{b}^{s+1}_{d-i,i-1,1} := -\mathbf{b}^s_{d-i,1,i-1} + 2\mathsf{c}\mathbf{b}^s_{d-i,0,i} + 2(1-\mathsf{c})\mathbf{b}^s_{d-i+1,0,i-1}, \quad i=1,\ldots,d \tag{3}$$

$$C^2 \text{ if } \quad \mathbf{b}^{s+1}_{d-i,i-2,2} := \mathbf{b}^s_{d-i,2,i-2} - 4\mathsf{c}\mathbf{b}^s_{d-i,1,i-1} + 4\mathsf{c}^2\mathbf{b}^s_{d-i,0,i} - 4(1-\mathsf{c})\mathbf{b}^s_{d-i+1,1,i-2} + 8\mathsf{c}(1-\mathsf{c})\mathbf{b}^s_{d-i+1,0,i-1} + 4(1-\mathsf{c})^2\mathbf{b}^s_{d-i+2,0,i-2}, \quad i=2,\ldots,d. \tag{4}$$

across the *sector boundary* between patch s and patch $s+1$ (modulo n). In the following,
– superscript s denotes the sector, i.e. $s \in \{0, 1, \ldots, n-1\}$ and
– superscript r denotes the refinement level, i.e. $r = 0, 1, \ldots$.

The six BB-coefficients $\mathbf{b}^0_{ijk}$ (indicated as red bullets in Fig. 5) define a quadratic expansion $\mathbf{q}$ at the central point $\mathbf{b}^0_{d00}$. This local expansion is propagated to the neighboring sectors by repeatedly enforcing Eq. (2) for $i = 0, 1, 2$, Eq. (3) for $i = 1, 2$ and Eq. (4) for $i = 2$. That is, the $\mathbf{b}^0_{ijk}$ define a unique quadratic expansion of the C^1 map $\mathbf{b}^{\triangle}$ at $\mathbf{b}^0_{d00}$.

With the quadratic expansion fixed, the C^1 constraints (3) can be rewritten as

$$\mathbf{b}^s_{d-i,0,i} := \frac{1}{2\mathsf{c}}\left(\mathbf{b}^s_{d-i,1,i-1} + \mathbf{b}^{s+1}_{d-i,i-1,1}\right) + \left(1 - \frac{1}{\mathsf{c}}\right)\mathbf{b}^s_{d-i+1,0,i-1}, \quad i = 3, \ldots, d. \tag{3'}$$

This allows the BB-coefficients

$$\mathbf{b}^s_{\restriction} := \{\mathbf{b}^s_{112}, \mathbf{b}^{s+1}_{121}, \mathbf{b}^{s+1}_{031}, \mathbf{b}^s_{013}\} \text{ of } \mathbf{b}^{\triangle}$$

to be unrestricted by C^1 continuity (see Fig. 5b); $\mathbf{b}^s_{022}$ is unrestricted due to its distance from the sector boundary.

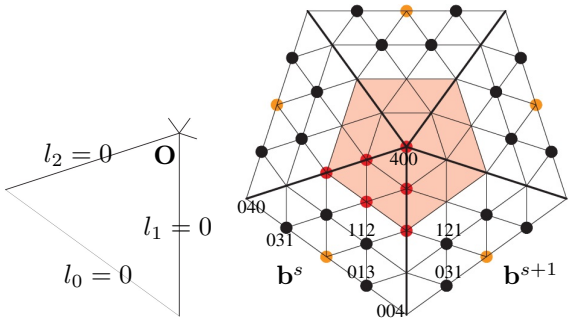

(a) domain (b) $\mathbf{b}^{\triangle}$

Figure 5: (a) Domain of total degree d map. (b) The $n = 5$ sectors of the C^1 map $\mathbf{b}^{\triangle}$ of degree $d = 4$. The 'light red' shaded region indicates the quadratic expansion $\mathbf{q}$ at the center. The BB-coefficients that remain unrestricted when enforcing C^1 constraints are marked as (black and red) bullets; the BB-coefficients shown as orange bullets do not affect C^1 continuity between sectors.

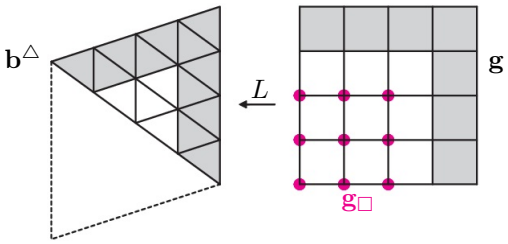

Figure 6: Increasing the flexibility of $\mathbf{b}^{\triangle}$ via linear shear L.

2.3. *The linear shear map L*

We denote by L the linear shear that maps a unit square to the unit parallelogram with opening angle $\frac{2\pi}{n}$ as illustrated in Fig. 6. To increase the flexibility we set for each sector

$$\mathbf{g} := \mathbf{b}^{\triangle} \circ L. \tag{5}$$

Then, see Fig. 6, along the sector boundary the gray-underlaid BB-coefficients of the C^1 map $\mathbf{b}^{\triangle}$ determine the corresponding gray underlaid BB-coefficients of the G^1 map $\mathbf{g}$. But while each sector of $\mathbf{b}^{\triangle}$ has only one coefficient not influencing C^1 continuity between sectors, each sector of $\mathbf{g}$ has 9 coefficients that do not influence G^1 continuity of $\mathbf{g}$. These coefficients, later referenced as $\mathbf{g}_{\square}$ (magenta bullets) provide extra degrees of freedom. Therefore $\mathbf{g}$ has a total of $9n + 4n + 6 = 13n + 6$ degrees of freedom.

Fig. 7a displays the sectors of $\mathbf{g}$ disjoint to emphasize that the guide is sampled *locally* in each sector, while subsequent adjustments are *local* respect to each sector boundary. Fig. 7b displays the BB-coefficients of $\mathbf{b}^{\triangle}$ that defines the gray underlaid BB-coefficients of $\mathbf{g}$ (unrestricted coefficients as bullets).

The switch from C^1 to G^1 maps (and later, via sampling in Section 4, back to C^1 maps) not only increases the freedom for the guide to achieve better shape but also connects guided subdivision to conventional subdivision, see Section 5. The complexity of such composition and re-sampling is reduced by defining local linear operators that apply to groups of coefficients as explained in Section 3.

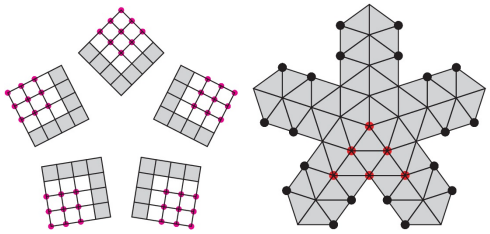

(a) sectors of $\mathbf{g}$ (b) $\mathbf{b}^{\triangle}$ coefficients determining gray part of $\mathbf{g}$

Figure 7: Multi-sector ($n = 5$) schema of (a) a collection of the sectors of the guide $\mathbf{g}$ and (b) the part of $\mathbf{b}^{\triangle}$ that determines the gray layers of BB-coefficients of $\mathbf{g}$.

2.4. *Characteristic parameterizations χ and $\tilde{\chi}$*

Fig. 8a displays the BB-coefficients of one sector of the characteristic map χ of Catmull-Clark subdivision (for $n = 5$). One way to obtain the gray-underlaid BB-coefficients is by subdividing a coarser L-shaped *tensor-border* $\tilde{\chi}$ of degree 3 and depth 2, shown in Fig. 8b. $\tilde{\chi}$ exists since the characteristic map χ, scaled by subdominant eigenvalue of Catmull-Clark subdivision, is C^2 connected to χ. We use $\tilde{\chi}^{\square} := L^{-1} \circ \tilde{\chi}$ to jet-sample $\mathbf{g}$ in each sector at the locations marked as crosses in Fig. 8c to form a tensor-border $\mathbf{t}$ as illustrated in Fig. 3d. The BB-coefficients marked solid blue or cyan in Fig. 3d are expressed as an affine combination of the gray-underlaid BB-coefficients of $\mathbf{g}$ and so of the gray underlaid coefficients of $\mathbf{b}^{\triangle}$. Since $\mathbf{g} := \mathbf{b}^{\triangle} \circ L$ and $\tilde{\chi}^{\square} := L^{-1} \circ \tilde{\chi}$ these BB-coefficients are directly calculated from the jet-sample $[\mathbf{b}^{\triangle} \circ \tilde{\chi}]$.

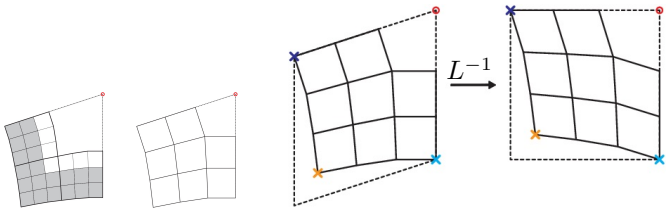

(a) χ (b) $\tilde{\chi}$ (c) $\tilde{\chi}^{\square} := L^{-1} \circ \tilde{\chi}$

Figure 8: One sector of (a) the characteristic parameterizations, (b) the characteristic tensor-border and (c) the usage of $\tilde{\chi}$.

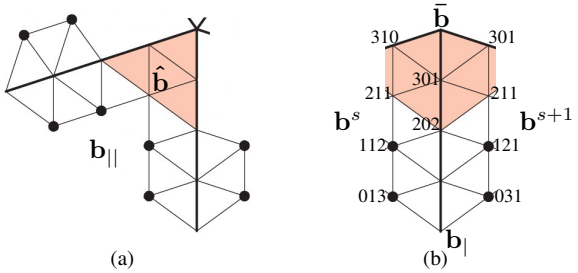

(a) (b)

Figure 9: Groups of BB-coefficients of $\mathbf{b}^{\triangle}$ (a) $\hat{\mathbf{b}}$ and $\mathbf{b}_{||}$ local to a segment and (b) $\mathbf{b}_{|}$ and $\bar{\mathbf{b}}$ local to a sector boundary.

3. Construction of the guide $\mathbf{g}$

The idea of separating detail from global shape, expressed by a guide surface, goes back at least to [9]. Since then the 'technology' for determining the guide and sampling it for the final surface have dramatically improved. For the construction, we form and operate on groups of BB-coefficients. Since the groups are local, we drop the superscript s that denotes the sector wherever this is unambiguous.

- $\hat{\mathbf{b}}$: per sector of $\mathbf{b}^{\triangle}$, the 6 BB-coefficients of the quadratic expansion $\mathbf{q}$ (light-red underlay in Fig. 9a).
- $\mathbf{b}_{|}$: per sector boundary of $\mathbf{b}^{\triangle}$, the 4 BB-coefficients $\mathbf{b}^s_{013}, \mathbf{b}^{s+1}_{031}, \mathbf{b}^s_{112}, \mathbf{b}^{s+1}_{121}$, see Fig. 9b.
- $\mathbf{b}_{||}$: per sector of $\mathbf{b}^{\triangle}$, the 8 BB-coefficients of the union of two $\mathbf{b}_{|}$ arrangements, see Fig. 9a.
- $\bar{\mathbf{b}}$: per sector boundary of $\mathbf{b}^{\triangle}$, 7 BB-coefficients of the quadratic expansion of $\mathbf{b}^{\triangle}$: $\mathbf{b}^s_{400}, \mathbf{b}^s_{301}, \mathbf{b}^s_{202}, \mathbf{b}^s_{310}, \mathbf{b}^{s+1}_{301}, \mathbf{b}^s_{211}, \mathbf{b}^{s+1}_{211}$, see Fig. 9b.
- $\mathbf{g}_{\square}$: per sector of $\mathbf{g}$, the 9 BB-coefficients (magenta bullets in Fig. 6) that do not affect the G^1 continuity between sectors.

We will determine the $13n+6$ BB-coefficients of $\mathbf{g}$ that are unrestricted by smoothness so that (parts of) the $\mathbf{g}$-sampled tensor-border $\mathbf{t}$ match (parts of) an incoming tensor-border $\mathbf{h}$. This elimination will be symbolic, i.e for unspecified $\mathbf{h}$ so as to obtain formulas that can be tabulated as a linear transformation matrix. The grouping of $\mathbf{t}$ and $\mathbf{h}$ is analogous to that of $\mathbf{b}^{\triangle}$ and $\mathbf{g}$ (see Fig. 10):

- $\mathbf{t}_{|}$ ($\mathbf{h}_{|}$) : per sector boundary, the 4 BB-coefficients with indices $\{30, 03, 31, 13\}$.
- $\mathbf{t}_{||}$ ($\mathbf{h}_{||}$) : per sector, the 8 BB-coefficients of the union of two $\mathbf{t}_{|}$ ($\mathbf{h}_{|}$) arrangements.
- $\mathbf{t}_{\square}$ ($\mathbf{h}_{\square}$) : per sector, the 9 BB-coefficients per sector with indices $i, j, 0 \le i, j \le 2$.

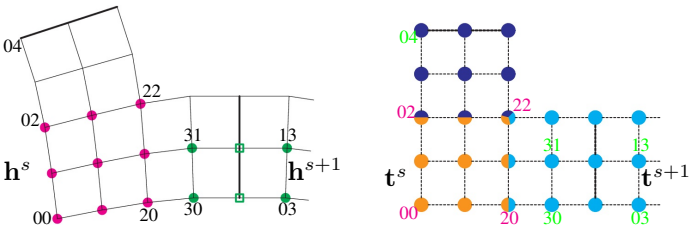

(a) incoming tensor-border $\mathbf{h}$ (b) sampled tensor-border $\mathbf{t}$

Figure 10: (a) An incoming tensor-border $\mathbf{h}$. (b) Tensor-border $\mathbf{t}$ sampled from $\mathbf{g}$.

Local linear operators. The following *linear* and *local operators* O_i map the groupings (in symbolic, non-numeric representation) into one another:
$O_1(\mathbf{h}_{|}, \bar{\mathbf{b}}) \to \mathbf{b}_{|}$: Express $\mathbf{b}_{|}$ as an affine combination of $\mathbf{h}_{|}$ and $\bar{\mathbf{b}}$ – so that $\mathbf{t}_{|} = \mathbf{h}_{|}$. (Due to the G^1 continuity of $\mathbf{g}$, the two BB-coefficients of $\mathbf{t}$ on sector boundary are $\frac{1}{2}(\mathbf{t}^s_{3i} + \mathbf{t}^{s+1}_{i3})$, $i = 0, 1$, hence coincide with the corresponding BB-coefficients of

$\mathbf{h}$ marked as hollow green boxes in Fig. 10a.)
$O_2(\mathbf{h}_\square, \mathbf{b}_{||}, \hat{\mathbf{b}}) \to \mathbf{g}_\square$: Express $\mathbf{g}_\square$ as an affine combination of $\mathbf{h}_\square$, $\mathbf{b}_{||}$, $\hat{\mathbf{b}}$ – so that $\mathbf{h}_\square = \mathbf{t}_\square$.
Applying O_1 to both boundaries of a sector and subsequently applying O_2 yields
$O_3(\mathbf{h}_\square, \mathbf{h}_{||}, \hat{\mathbf{b}}) \to \mathbf{g}_\square$: analogous to O_2 but with $\mathbf{h}_{||}$ in place of $\mathbf{b}_{||}$.

Note that O_1 is local to a pair of sectors and O_2, O_3 thereafter are local to one sector. The operators are 'invertible' in the sense that we can equally well determine

$$O_1'(\mathbf{b}_|, \bar{\mathbf{b}}) \to \mathbf{h}_|, \quad O_2'(\mathbf{g}_\square, \mathbf{b}_{||}, \hat{\mathbf{b}}) \to \mathbf{h}_\square. \tag{6}$$

Leveraging the substitution operators O_1 and O_3, we get that $\mathbf{t}_\square = \mathbf{h}_\square$ and $\mathbf{t}_| = \mathbf{h}_|$, i.e. we almost match the incoming tensor-border $\mathbf{h}$ with the sampled tensor-border $\mathbf{t}$, for any choice of the 6 BB-coefficients in quadratic expansion $\mathbf{q}$.

Guide construction. Since the incoming tensor-border $\mathbf{h}$ is an affine combination of the $\mathbf{c}$-net, the above operators express the BB-coefficients of $\mathbf{g}$ linearly in terms of the $\mathbf{c}$-net and the quadratic expansion $\mathbf{q}$. We set the central BB-coefficient $\mathbf{b}^0_{400}$ in terms of the $\mathbf{c}$-net (see Fig. 11, $\mathbf{c}^k_7$, $k = 0, \ldots, n-1$, is the central node)

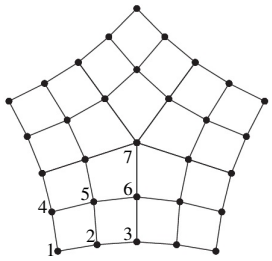

Figure 11: Rotationally-symmetric labelling of one sector of the $\mathbf{c}$-net.

$$\text{if } n > 4, \quad \frac{n}{n+5}\mathbf{c}^0_7 + \sum_{k=0}^{n-1}(\gamma_5 \mathbf{c}^k_5 + \gamma_6 \mathbf{c}^k_6), \tag{7}$$
$$\gamma_5 := \frac{1}{n(n+5)}, \quad \gamma_6 := 4\gamma_5,$$
$$\text{if } n = 3, \quad (1 - 3\gamma_5 - 3\gamma_6)\mathbf{c}^0_7 + \sum_{k=0}^{2}(\gamma_5 \mathbf{c}^k_5 + \gamma_6 \mathbf{c}^k_6), \tag{8}$$
$$\gamma_5 := \frac{5}{96}, \ \gamma_6 := \frac{1}{6},$$

i.e. as the extraordinary point of Catmull-Clark subdivision except for a small perturbation to improve shape when $n = 3$. The remaining BB-coefficients $\Gamma := \{\mathbf{b}^0_{310}, \mathbf{b}^0_{301}, \mathbf{b}^0_{220}, \mathbf{b}^0_{211}, \mathbf{b}^0_{202}\}$ determine the quadratic expansion and are fixed by minimizing

$$\min_\Gamma \sum_{s=0}^{n-1} \mathcal{F}_4(\mathbf{g}^s), \quad \mathcal{F}_k f := \int_0^1 \int_0^1 \sum_{\substack{i+j=k \\ i,j\geq 0}} \frac{k!}{i!j!}(\partial_s^i \partial_t^j f)^2 ds dt. \tag{9}$$

Implementation of $\mathbf{g}$ via generating functions. The initialization works for each coordinate separately. When all nodes of $\mathbf{c}$-net have value 0, except that $\mathbf{c}^0_m = 1$ for one of $m = 1, \ldots, 7$ (see Fig. 11), we obtain the scalar-valued bi-4 coefficients

$$h^{k,m}_{ij} \in \mathbb{R}, \ k = 0, \ldots, n-1, \ m = 1, \ldots, 7, \ i, j \in \{0, \ldots, 4\},$$

where $h^{0,7}_{ij} = \ldots = h^{n-1,7}_{ij}$. Then the BB-coefficients of $\mathbf{g}$ are

$$\mathbf{g}^s_{ij} := h^{0,7}_{ij}\mathbf{c}^0_7 + \sum_{k=0}^{n-1}\sum_{m=1}^{6} h^{k,m}_{ij}\mathbf{c}^{s-k}_m,$$

where the superscript of $\mathbf{c}^{s-k}_m$ is interpreted modulo n.

3.1. A C^2 bi-4 transition ring

If we choose $\mathbf{h} = \mathbf{t}_{CC}$ (see Section 2.1) then the highlight line distributions of guided subdivision surfaces are better than those of Catmull-Clark subdivision. However for some challenging configurations (see Section 8) the transition from input bi-3 data to the first guided ring is noticeable in the highlight lines. This can be traced back to the fact that the sampled tensor-border $\mathbf{t}$ does not reproduce the entire $\mathbf{t}_{CC}$. To smooth out the transition, we could apply Catmull-Clark-refinement. However Catmull-Clark subdivision's tendency to pinch highlight lines often damages the shape already in a single refinement (see Fig. 27).

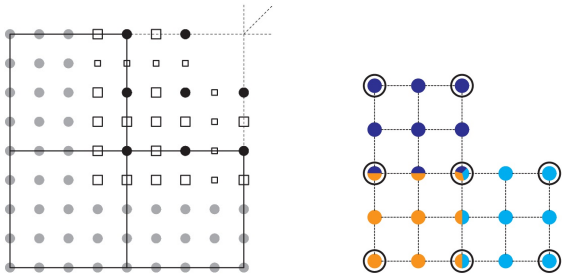
(a) C^2 bi-4 patches (b) sampled $\mathbf{t}$

Figure 12: (a) Structure of transition bi-4 ring. (b) tensor-border $\mathbf{t}$ sampled from $\mathbf{g}_5$. Its circled coefficients are picked as the coefficients shown as black bullets in (a).

To remove the first-step artifacts from the highlight line distribution, we insert one C^2 bi-4 ring $\mathbf{x}_{tran}$. This transition ring has the same layout as those of Catmull-Clark subdivision. Using the C^2 prolongation of $\mathbf{x}_{tran}$ as incoming tensor-border $\mathbf{h}$ makes the transition defects disappear. The transition ring is constructed as follows (see Fig. 12):

- The outer BB-coefficients (gray bullets in Fig. 12a) are the tensor-border $\mathbf{t}_{CC}$ once split.
- The tensor-border $\mathbf{t}$ (see Fig. 12b) is assembled as in Section 3 but with jets $[\mathbf{g}_5 \circ (\lambda\tilde{\chi}^\square)]^4_{3\times 3}$. The map $\mathbf{g}_5$ detailed in the Appendix mimics $\mathbf{g}$ but better captures $\mathbf{t}_{CC}$.
- The circled coefficients of $\mathbf{t}$ become those marked by black bullets in Fig. 12a.
- The C2-rule enforces C^2 connection to the finer layer by first determining every second BB-coefficient (marked as big hollow squares in Fig. 12a) from those marked as black and grey bullets; and then those marked as small hollow squares.

For efficient implementation via generating functions, only 6 entries need to be pre-computed (for 6 of the 8 black bullets that can be assigned to one sector and are not covered by the neighbor sector Fig. 12a).

4. Subdivision surfaces guided by g

Each subdivision step consists of jet-sampling the guide and smoothly joining the resulting jet information. Note that in the following the superscript r in $\mathbf{t}^r$ denotes the refinement level and the superscript s for sector need not be mentioned as it is clear from the context. Recall that for best shape, we insert a transition ring $\mathbf{x}_{tran}$. The C^2 prolongation of $\mathbf{x}_{tran}$ is therefore the incoming tensor-border $\mathbf{t}^0 := \mathbf{h}$ for constructing $\mathbf{g}$.

4.1. Sampling with $\tilde{\chi}^{\square}$

Analogous to Section 3, we create tensor-borders $\mathbf{t}^r$, $r > 0$ by assembling three corner jets $[\mathbf{g} \circ (\lambda^r \tilde{\chi}^{\square})]_{3\times 3}^4$, averaged where they overlap (see Fig. 3d). Here λ is the subdominant eigen-value of CC subdivision and Fig. 13 shows $\tilde{\chi}^{\square}$ and its scaled copy $\lambda\tilde{\chi}^{\square}$.

Computing $[\mathbf{g}\circ(\lambda\tilde{\chi}^{\square})]_{3\times 3}^4$ is equivalent to linearly mapping $S : [0..1]^2 \to [0..\lambda]^2$ and sampling $(\mathbf{g}\circ S)\circ\tilde{\chi}^{\square}$. De Casteljau's algorithm at $u = \lambda = v$ yields the BB-coefficients of $\mathbf{g} \circ S$ as the affine combinations of BB-coefficients of $\mathbf{g}$ and these are easy to tabulate: due to combinatorial symmetry of construction only one affine $5^2 \times 5^2$ map (de Casteljau) and one 21×5^2 map (sampling of $\mathbf{t}^1$) are required.

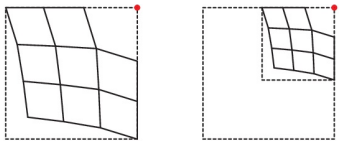

Figure 13: Scaled sampling. The origin is marked red.

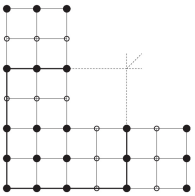

Figure 14: Correction of C^1 $\mathbf{t}^r$ to C^2 $\tilde{\mathbf{t}}^r$.

4.2. Constructing guided rings

The sectors of the sampled tensor-borders $\mathbf{t}^r$ are automatically C^1 connected. Applying the C2-rule joins the sectors C^2. (This smoothing allows reducing the size of the $\mathbf{t}^1$ sampling map to 12×5^2: 9 entries for $\mathbf{t}_{\square}$ and 3 on the sector boundary.) The C^2 tensor-border is called $\tilde{\mathbf{t}}^r$ (see Fig. 14), and since the sectors of $\mathbf{h}$ are C^2 connected $\tilde{\mathbf{t}}^0 = \mathbf{t}^0$. Then $\tilde{\mathbf{t}}^r$ and $\tilde{\mathbf{t}}^{r+1}$ determine the r-th ring $\mathbf{x}^r$, $r = 0, 1, \ldots$ as follows.

4.2.1. C^1-joined rings

To join consecutive rings C^1 (see Fig. 15a) the 'outer' dark-gray underlaid BB-coefficients of the three bi-4 patches of a sector of $\mathbf{x}^r$ are those of $\tilde{\mathbf{t}}^r$ (once subdivided). The ring joins C^1 to the tensor-border $\tilde{\mathbf{t}}^{r+1}$ by choice of the light-gray underlaid BB-coefficients of $\mathbf{x}^r$. Then the sequence of rings is C^2-connected to the input data, the neighbor sectors join C^2 and the dark-gray all underlaid layers of $\mathbf{x}^r$ are C^2 connected with one another within the ring.

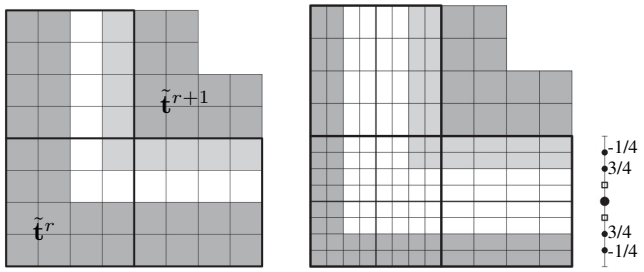

(a) C^1 prolongation (b) C^2 prolongation

Figure 15: Structure of the guided bi-4 rings. The dark-gray underlaid BB-coefficients are those of $\tilde{\mathbf{t}}^r$ and, in the upper right, of $\tilde{\mathbf{t}}^{r+1}$. Light-gray BB-coefficients ensure smoothness.

4.2.2. C^2-joined rings

Alternatively, we can join consecutive rings C^2. Each sector of $\mathbf{x}^r$ is split into $4 + 2 + 2$ patches of degree bi-4 (see Fig. 15b). Again the 'outer' dark-gray underlaid BB-coefficients are those of $\tilde{\mathbf{t}}^r$, suitably split. The ring joins C^2 to the tensor-border $\tilde{\mathbf{t}}^{r+1}$ by choice of the light-gray underlaid BB-coefficients of $\mathbf{x}^r$. Internal C^2 joints are computed using the stencil to the right of Fig. 15b that determines the boundary coefficient (big black bullet) as an affine combination of the smaller bullets (with the displayed weights). We set their neighbors (hollow boxes) via the C2-rule. This yields two once-split patches and (tensoring the split) one 2×2 corner patch per sector of $\mathbf{x}^r$. Each such macro-patch is internally C^3.

5. Reformulating bi-4 guided subdivision towards traditional small-stencil subdivision

Despite the obvious similarities to subdivision using small stencils, such as CC subdivision [5], guided subdivision appears to differ from traditional subdivision:
(i) the B-spline-like control net only serves to initialize the guide. Thereafter, rings are controlled by the guide, not the net.
(ii) Although the contracting guided rings follow rules that are efficient due to scalability and pre-calculation, these guided rules are clearly more complicated than traditional stencils: the refinement matrix of guided subdivision is less sparse.

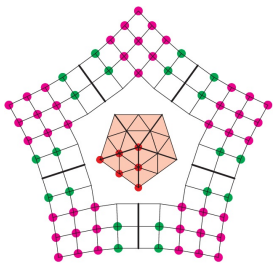

Figure 16: New determining set of $\mathbf{g}$: $\mathbf{t}_{\square}$, $\mathbf{t}_{|}$, and quadratic expansion (6 red bullets).

We therefore reformulate the guide construction of Section 3 and the guided subdivision of Section 4 to better resemble traditional subdivision rules. The final rules map tensor-borders to

tensor-borders and are tabulated for each valence n. The new determining set is illustrated in Fig. 16. *Wrapping* the original bi-4 guided subdivision of Section 4 by applying operators O_1, O_2, O_1' and O_2' allows replacing $\mathbf{b}_|, \mathbf{g}_\square$ by $\mathbf{t}_| = \mathbf{h}_|, \mathbf{t}_\square = \mathbf{h}_\square$. The quadratic expansion (underlaid light-red) remains unchanged:
– apply O_1 and O_3 (to restore the original determining set of $\mathbf{g}$);
– compute $\mathbf{g} \circ S$ (as in Section 4.1);
– apply O_1' and O_2' (to re-create the new determining set of $\mathbf{g}$).
This yields alternative *local linear subdivision operators* R_i:

- $R_1(\mathbf{t}_|^r, \bar{\mathbf{b}}^r) \to \mathbf{t}_|^{r+1}$: Symbolically express $\mathbf{t}_|^{r+1}$ as affine combination of $\mathbf{t}_|^r$ and of $\bar{\mathbf{b}}^r$.
- $R_2(\mathbf{t}_\square^r, \mathbf{t}_{||}^r, \hat{\mathbf{b}}^r) \to \mathbf{t}_\square^{r+1}$: Symbolically express $\mathbf{t}_\square^{r+1}$ as an affine combination of $\mathbf{t}_\square^r$, $\mathbf{t}_{||}^r$, $\hat{\mathbf{b}}^r$,

where the superscript r indicates the refinement level. For a given n, R_1 can be tabulated as a matrix of size 4×11 and R_2 as a matrix of size 9×23.

- Since $L \circ S \circ L^{-1}$ amounts to scaling of D by λ with respect to the origin, the refinement formulas for $\hat{\mathbf{b}}$ (see Fig. 17) are

$$\begin{aligned}
\hat{\mathbf{b}}_{400}^{r+1} &:= \hat{\mathbf{b}}_{400}^r, \qquad \hat{\mathbf{b}}_{310}^{r+1} := (1-\lambda)\hat{\mathbf{b}}_{400}^r + \lambda \hat{\mathbf{b}}_{310}^r, \\
\hat{\mathbf{b}}_{220}^{r+1} &:= (1-\lambda)^2 \hat{\mathbf{b}}_{400}^r + 2(1-\lambda)\lambda \hat{\mathbf{b}}_{310}^r + \lambda^2 \hat{\mathbf{b}}_{220}^r, \\
\hat{\mathbf{b}}_{211}^{r+1} &:= (1-\lambda)^2 \hat{\mathbf{b}}_{400}^r + (1-\lambda)\lambda(\hat{\mathbf{b}}_{310}^r + \hat{\mathbf{b}}_{301}^r) + \lambda^2 \hat{\mathbf{b}}_{211}^r.
\end{aligned} \tag{10}$$

  $\hat{\mathbf{b}}_{301}^{r+1}$ and $\hat{\mathbf{b}}_{202}^{r+1}$ are defined by mirrored formulas. Since $\bar{\mathbf{b}}$ consists of pieces of neighboring $\hat{\mathbf{b}}$, the formulas also define the refinement of $\bar{\mathbf{b}}$.

Wrapping also the sampled tensor-border construction (apply O_1 and O_3, jet-sample to obtain the tensor-border $\mathbf{t}$, apply O_1' and O_2') yields an operator $O_4(\mathbf{t}_|^r, \bar{\mathbf{b}}^r) \to \mathbf{t}_{ij}^r, ij \in \{32, 23\}$ that expresses the coefficients marked as big bullets in Fig. 18 as a linear combination of $\mathbf{t}_|^r$ (small bullets) and $\bar{\mathbf{b}}^r$. For each n, this operator can be tabulated as a 2×11 matrix. Setting the shared BB-coefficients on the sector boundary (marked as the hollow squares in Fig. 18) as averages completes the tensor-border $\mathbf{t}^r$. With the tensor-borders $\mathbf{t}^{r-1}$ and $\mathbf{t}^r$ known, we can proceed as in Section 4.2 to complete and join the rings C^1 or C^2.

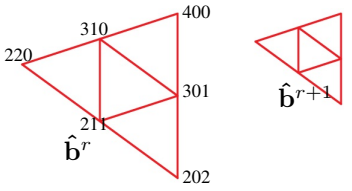

Figure 17: Refinement of the quadratic expansion.

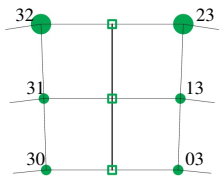

Figure 18: Completing $\mathbf{t}^r$ beyond $\mathbf{t}_|^r$.

By construction, the *reformulated* guided bi-4 subdivision surface is identical to the *original* constructed according to Section 4.2. However, there are several benefits to the reformulated version. The original scheme requires storing $\mathbf{g}$, i.e. the coefficients $h_{ij}^{k,m}$, $i, j \in \{0, \ldots, 4\}$ of Section 3 while the reformulated scheme requires storing only the quadratic expansion, i.e. $h_{ij}^{k,m}$, $i + j \le 2$ since

$$\begin{aligned}
&\mathbf{b}_{400} = \mathbf{g}_{00},\ \mathbf{b}_{310} = \mathbf{g}_{10},\ \mathbf{b}_{301} = \mathbf{g}_{01},\ \mathbf{b}_{220} = \mathbf{g}_{20}, \\
&\mathbf{b}_{202} = \mathbf{g}_{02},\ \mathbf{b}_{211} = \frac{1}{3}\big(\mathbf{g}_{00} - \mathbf{g}_{10} - \mathbf{g}_{01} + 4\mathbf{g}_{11}\big).
\end{aligned}$$

And since the reformulated rules require fewer arithmetic operations its evaluation is faster.

6. Eigen-structure of guided bi-4 surfaces

While, for applications, we suggest capping the subdivision after a few steps, a complete theoretical analysis is possible.

6.1. *The guide* $\mathbf{g}$ *as a superposition of homogeneous functions*

The Bernstein polynomials $B_{0jk}^d := \binom{d}{0jk} l_1^j l_2^k$ are homogeneous of degree d: for any λ, $B_{0jk}^d(\lambda x) = \lambda^d B_{0jk}^d(x)$. Consequently $B_{0jk}^d \circ L$, of degree $j \times k$, is homogeneous of degree d: for any λ,

$$(B_{0jk}^d \circ L)(\lambda u, \lambda v) = \lambda^d (B_{0jk}^d \circ L)(u, v).$$

Homogeneity is not affected by constraints (2–4). If we set one unconstrained BB-coefficient to 1 and the others to 0, the resulting $\mathbf{g}$ is homogeneous in all sectors. These simple observations allow to efficiently construct an explicit basis of homogeneous functions of the guide $\mathbf{g}$. We count

– 6 functions corresponding to the quadratic expansion: the function 1, two of degree 1 and three of degree 2.
– The $4n$ functions that are non-zero on two adjacent sectors: $2n$ of degree 3 and $2n$ of degree 4.
– $9n$ functions (n groups of 9) that are non-zero only in one sector: $B_{022}^4 \circ L$ of degree 4, $B_{032}^5 \circ L$, $B_{023}^5 \circ L$ of degree 5, $B_{042}^6 \circ L$, $B_{033}^6 \circ L$, $B_{024}^6 \circ L$ of degree 6, $B_{043}^7 \circ L$, $B_{034}^7 \circ L$ of degree 7 and $B_{044}^8 \circ L$ of degree 8.

Scaling the arguments of $\mathbf{g}$ by any λ therefore scales n_ν basis functions by λ^ν:

$\nu =$	0	1	2	3	4	5	6	7	8
$n_\nu =$	1	2	3	$2n$	$3n$	$2n$	$3n$	$2n$	n.

(11)

6.2. *Eigen-structure of guided subdivision surfaces*

Both C^1 and C^2 bi-4 guided subdivision surfaces inherit the homogeneous decomposition of the guide $\mathbf{g}$. For analyzing the eigenstructure we start with ring $\mathbf{x}^1$ (skipping the transition ring $\mathbf{x}^0$ whose eigen-decomposition, by smooth extension from $\mathbf{x}^1$ is not complicated but would distract.) We denote by $\mathbf{x}_{d,p}^r$ the rth ring obtained applying the constructions of Section 4.2 to the pth homogeneous functions $\mathbf{f}_{d,p}$ of degree d in Section 6.1. By construction, $\mathbf{x}_{d,p}^r = (\lambda^d)^{r-1} \mathbf{x}_{d,p}^1$. (This means that we can, as in [10] and implicit in [11], pre-compute the initial $13n + 6$ eigen-rings $\mathbf{x}_{d,p}^1$ and obtain eigen-functions $\mathbf{x}_{d,p}^r$ by scaling with $(\lambda^d)^{r-1}$.)

The prominence of the homogeneous functions, closely related to monomials of the power form, re-affirms that the eigen-decomposition serves theoretical analysis; for modelling the BB-form is more suitable.

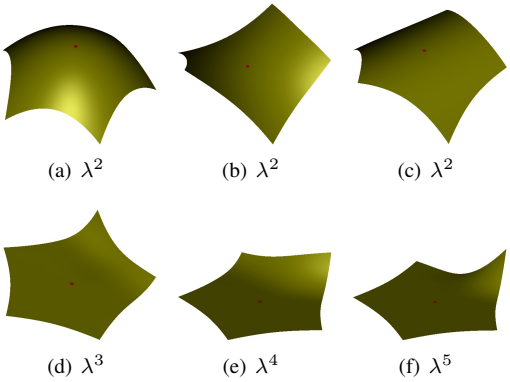

(a) λ^2 (b) λ^2 (c) λ^2

(d) λ^3 (e) λ^4 (f) λ^5

Figure 19: Eigenfunctions for $n = 5$.

Fig. 19 displays some C^1 bi-4 eigenfunctions for $n = 5$. Their C^2 counterparts are visually alike. We used χ for the planar abscissae and scaled vertically for a better visual impression. The tiny red center is the G^1 bi-4 cap to be constructed in Section 7. The *top*-row of Fig. 19 shows the eigenfunctions of elliptic, hyperbolic and parabolic shapes.

Smoothness at the extraordinary point. The linear combination of the two homogeneous eigen-functions of degree 1 reproduces χ. Since χ is injective [12], the eigen-spectrum (11) implies that the bi-4 guided subdivision surfaces are generically at least C^1 and curvature bounded.

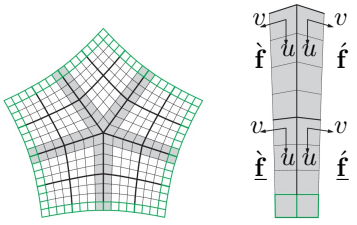

(a) central bi-4 cap (b) G^1 constraint

Figure 20: (a) Structure of the bi-4 cap. (b) BB-coefficients and u, v along the sector boundary involved in solving the G^1 constraints (12).

7. The central cap

The bi-4 central cap is formed by n 2×2 macro-patches. Each macro-patch is internally C^1 and joins C^1 with the sector of the last ring $\mathbf{x}_l$: the (split) C^1 prolongation defines the green underlaid BB-coefficients in Fig. 20a. The light-gray underlaid BB-coefficients

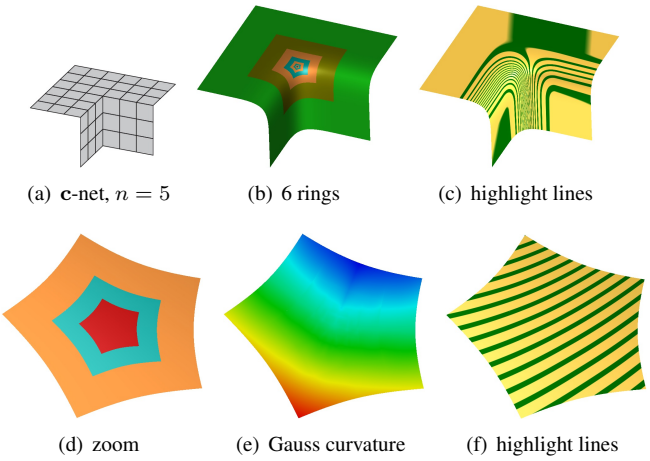

(a) **c**-net, $n = 5$ (b) 6 rings (c) highlight lines

(d) zoom (e) Gauss curvature (f) highlight lines

Figure 21: (b) The surrounding bi-3 surface data (green) is respected by the bi-4 transition bi-4 ring (bronze) and completed by $\bar{r} = 6$ bi-4 rings and red central cap. (c) highlight line distribution shows no artifacts across the transition (bronze). (d) Zoom to the last two rings and cap, (e) their Gauss curvature and (f) highlight lines.

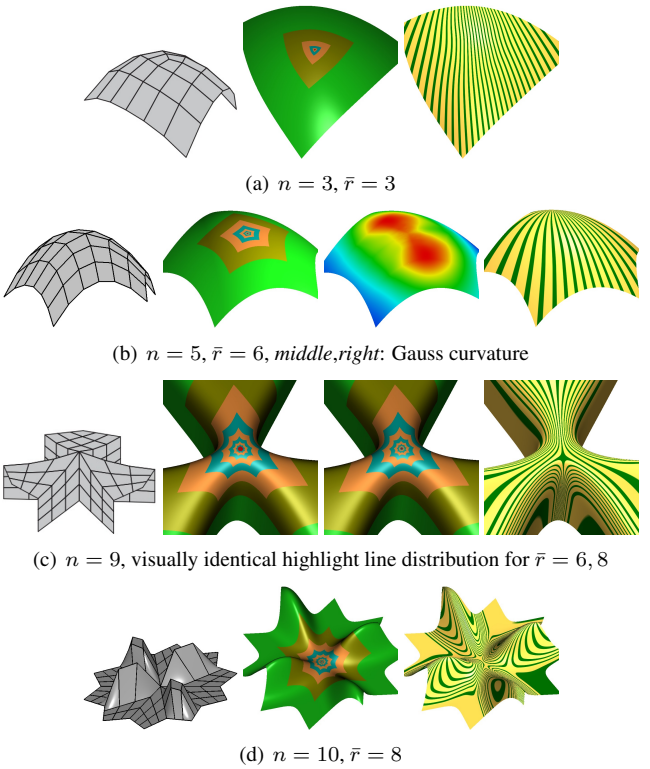

(a) $n = 3, \bar{r} = 3$

(b) $n = 5, \bar{r} = 6$, *middle*,*right*: Gauss curvature

(c) $n = 9$, visually identical highlight line distribution for $\bar{r} = 6, 8$

(d) $n = 10, \bar{r} = 8$

Figure 22: Part of the geometric obstacle course. (*left*) **c**-net. (*middle*) Bi-3 surrounding (green), bi-4 transition $\mathbf{x}_{tran}$ (bronze), guided bi-4 rings $\mathbf{x}^r$, $r = 0, \ldots, \bar{r} - 1$, and tiny red central cap. (*right*) highlight lines.

enforce the G^1 constraints of adjacent macro-patches (see Fig. 20b) for the subpatches $\underline{\grave{\mathbf{f}}}$, $\underline{\acute{\mathbf{f}}}$ attached to the last ring and the subpatches $\grave{\mathbf{f}}$, $\acute{\mathbf{f}}$ attached to the center:

$$\partial\grave{\mathbf{f}}_v + \partial\acute{\mathbf{f}}_v - (2\mathsf{c}(1-u) + \frac{2}{3}\mathsf{c}u)\partial\grave{\mathbf{f}}_u = 0, \qquad (12)$$
$$\partial\underline{\grave{\mathbf{f}}}_v + \partial\underline{\acute{\mathbf{f}}}_v - \frac{2}{3}\mathsf{c}(1-u)^2\partial\underline{\grave{\mathbf{f}}}_u = 0\,.$$

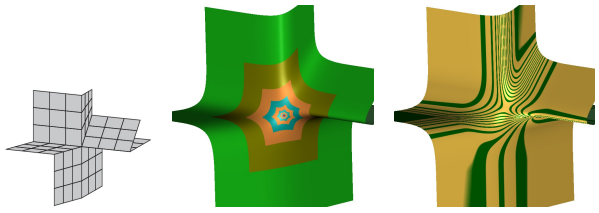

(a) **c**-net, $n = 7$ (b) structure (c) highlight lines

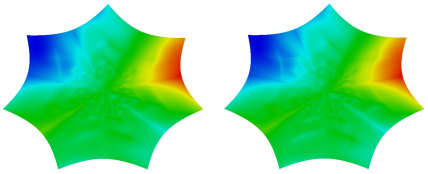

(d) C^2-joined rings (e) C^1-joined rings

Figure 23: Six rings plus cap for $n = 7$ input. The mean curvature differs little whether the rings join (d) C^2 or (e) C^1.

We form a preliminary bi-4 cap by sampling the guide (reparameterized to have the layout of the cap) as in Fig. 3c. BB-coefficients unconstrained by either C^1 or G^1 constraints are set to closely match those of the preliminary cap and the central cap inherits the quadratic expansion of the guide $\mathbf{g}$ at the central point. The symbolic calculations yield a tabulated matrix that allows efficient inclusion of the central cap into the guided framework.

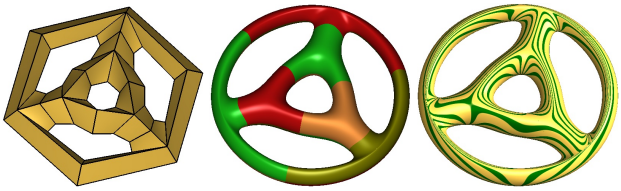

(a) $n = 6$, genus 4

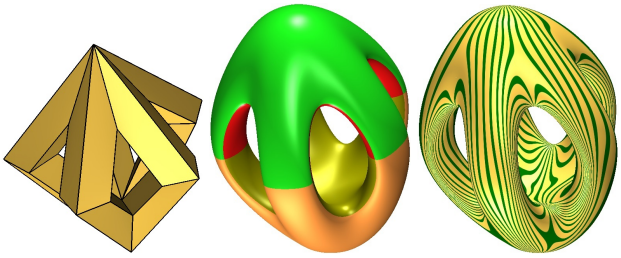

(b) $n = 10$, genus 4

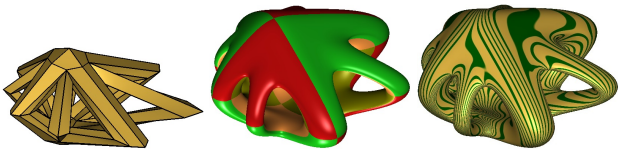

(c) $n = 7$, genus 7

Figure 24: (*left*) MSV meshes [13]. (*middle*) n-sided regions, shown in different colors, consist of one bi-4 transition ring, $\bar{r} = 6$ C^1 guided rings and a central cap. (*right*) highlight lines.

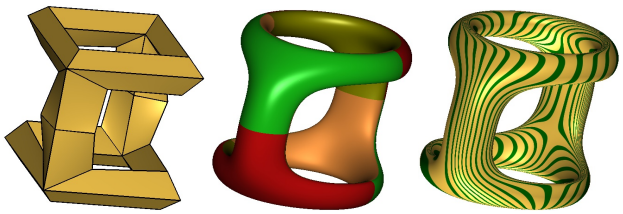

(a) MVS mesh, $n = 6$, $\bar{r} = 6$

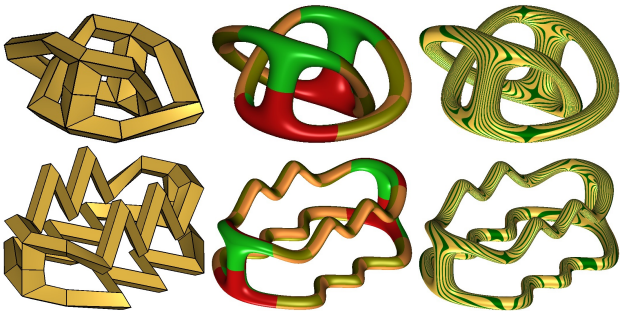

Figure 25: (*left*) meshes. (*middle*) surface layout. (*right*) highlight lines.

8. Examples

Fig. 21 demonstrates how the C^1 algorithm copes with a common two-beam corner configuration. Remarkably, the highlight line distribution is indistinguishable from that of the C^2 algorithm and the curvature distribution is alike! This similarity of the C^1 and C^2 bi-4 surfaces is confirmed by Fig. 23 for valence 7. Again the highlight line are indistinguishable and the curvature differences are negligible. More examples of good highlight line distributions for the geometric obstacle course [14] are shown in Fig. 22. Fig. 22c in particular demonstrates that higher valencies slow the contraction, hence require more subdivision rings for a tiny cap to be deployed. However visually, the two $n = 9$-sided surfaces are identical.

The input to Fig. 24 are MVS meshes in order to compare to a G^2 bi-4 construction with 2×2 patches per sector [13], called MVS surfaces. ([13] requires minimal single-valence, MSV, meshes consisting of vertices of a single irregular valence n, two of which are separated by exactly one regular, 4-valent vertex). Remarkably, the highlight line distribution and curvature of guided bi-4 construction are on par with that of the MVS G^2 surfaces. Since MVS surfaces are only G^1-refinable they are less suited for analysis than the guided bi-4 construction. Moreover, see Fig. 25, guided bi-4 construction can insert additional shape while MSV surfaces cannot (because they do not include regular bi-3 patches).

Fig. 26 demonstrates that the constructions without transition ring can fail to produce fair shape. For this configuration one Catmull-Clark refinement improves the situation, but Fig. 27 demonstrates that one Catmull-Clark refinement can severely damage the highlight line distribution of a convex configuration.

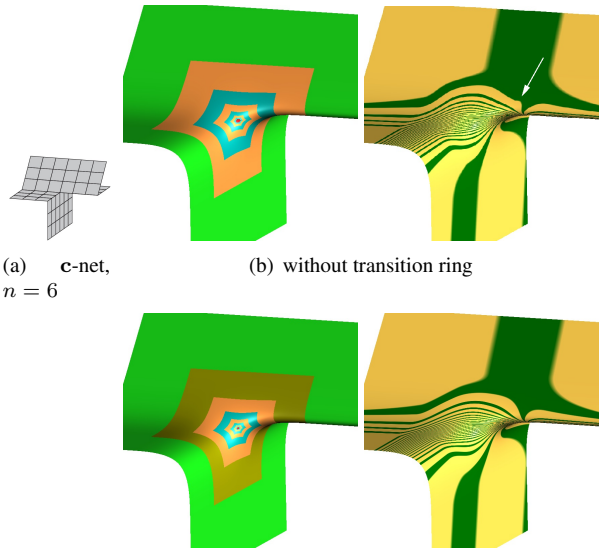

(a) **c**-net, $n = 6$ (b) without transition ring

(c) with (bronze) transition ring $\mathbf{t}_{tran}$

Figure 26: The ring sequence for $n = 6$ between the green input bi-3 ring and the red central cap (b,c,d) and their highlight line distribution. (b) No transition ring. Note the kink in the highlight lines (white arrow). (c) default construction with transition ring.

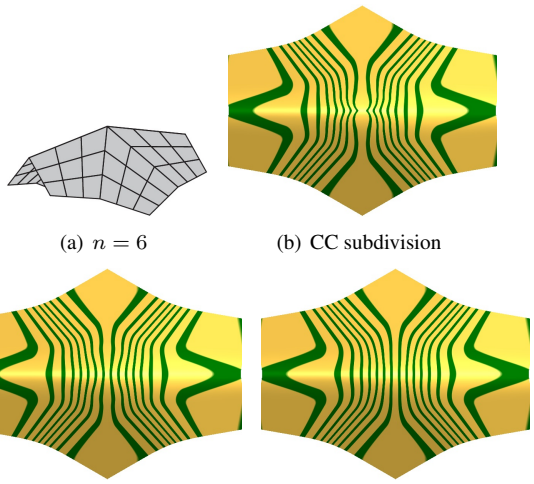

(a) $n = 6$ (b) CC subdivision

(c) bi-4 no transition ring, one CC step (d) bi-4 guided subdivision with default transition ring

Figure 27: Convex **c**-net, $n = 6$. The highlight shadings of corresponding surfaces: (b) Catmull-Clark subdivision; (c) bi-4 construction without transition ring after one Catmull-Clark refinement; (d) default construction with transition ring (no Catmull-Clark refinement).

Fig. 28 illustrates that a minimal valence $n = 3$ requires maximal care – motivating the choice (8) of the central point.

While refinable functions are primarily intended for analysis on the surface, not for geometry, Fig. 29 visualizes how the degrees of freedom arising from refinement can be used to modify the shape of guided subdivision surfaces at higher frequencies.

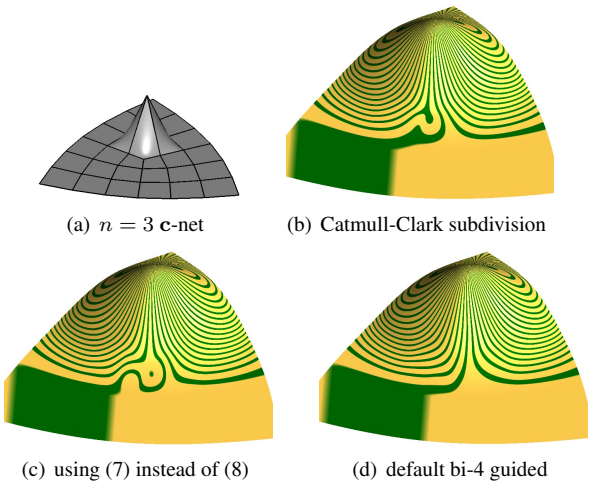

(a) $n = 3$ **c**-net (b) Catmull-Clark subdivision

(c) using (7) instead of (8) (d) default bi-4 guided

Figure 28: The highlight line distribution for $n = 3$ sectors of (b) Catmull-Clark subdivision (CC); (c) central point set to the extraordinary point of CC (7); (d) the default construction for $n = 3$ using (8).

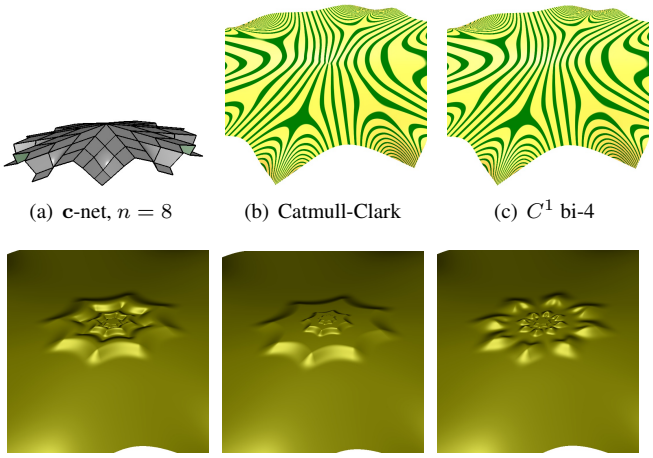

(a) **c**-net, $n = 8$ (b) Catmull-Clark (c) C^1 bi-4

(d) Manipulation of higher frequencies on consecutive subdivision rings

Figure 29: High valence and adaptive changes.

9. Conclusions

Compared to earlier guided subdivision schemes, the new bi-4 guided construction offers:
– Improved surface quality as measured by the highlight line distribution over an obstacle course of challenging examples.
– A remarkably simple eigen-structure characterized and determined by the guide.
– A conceptually simple construction and implementation based on local pre-calculated operators.

Compared to Catmull-Clark subdivision it can be pointed out that
– both are linear processes that generate inner surface rings from outer surface rings.
– The matrix of Catmull-Clark subdivision stencils is sparser. The local refinement operators of guided subdivision yield only a block-sparse matrix.
– While Catmull-Clark subdivision approximates a central node,

guided subdivision approximates a central quadratic derived from the input $\mathbf{c}$-net.
– The highlight line distribution of guided subdivision does not have the artifacts observed for Catmull-Clark subdivision.
– While we can generate a sequence of C^2-joined rings according to Section 4.2.2, our preference is to generate C^1-joined rings according to Section 4.2.1. The C^1-joined rings have a highlight line distribution and even curvature display on par with the C^2-joined rings but are structurally simpler.
The overall trade-off therefore appears to be as follows. By working directly with small refinement stencils on the $\mathbf{c}$-net, Catmull-Clark subdivision has an appealing, simple and intuitive mesh refinement. However, this simplicity yields a complex eigen-structure and sub-par highlight line distribution. By contrast, guided subdivision requires formulas that are too long to conveniently write out explicitly in terms of the $\mathbf{c}$-net; but the guided subdivision rings are observed to have a good highlight line distribution over a range of challenging inputs and a simple eigen-structure.

For practical use, a few bi-4 guided subdivision rings plus cap yield a finite number of polynomial pieces and so an automatic conversion of quad meshes with irregular vertices into high-quality surfaces with built-in refinability. This hybrid preserves the shape and is readily amenable to subsequent computations on the surface.

Acknowledgements. This work was supported in part by DARPA HR00111720031 and NIH R01 LM011300-01.

[1] D. Groisser, J. Peters, Matched G^k-constructions always yield C^k-continuous isogeometric elements, Computer Aided Geometric Design 34 (2015) 67–72.
[2] K. Karčiauskas, T. Nguyen, J. Peters, Generalizing bicubic splines for modelling and IGA with irregular layout, Computer Aided Design 70 (2016) 23–35.
[3] M. Kapl, G. Sangalli, T. Takacs, Dimension and basis construction for analysis-suitable G^1 two-patch parameterizations, Computer Aided Geometric Design 52 (2017) 75–89.
[4] K. Karčiauskas, J. Peters, Refinable G^1 functions on G^1 free-form surfaces, Computer Aided Geometric Design 54 (2017) 61–73.
[5] E. Catmull, J. Clark, Recursively generated B-spline surfaces on arbitrary topological meshes, Computer-Aided Design 10 (1978) 350–355.
[6] K.-P. Beier, Y. Chen, Highlight-line algorithm for realtime surface-quality assessment, Computer-Aided Design 26 (4) (1994) 268–277.
[7] G. Farin, Curves and Surfaces for Computer Aided Geometric Design: A Practical Guide, Academic Press, San Diego, 2002.
[8] H. Prautzsch, W. Boehm, M. Paluszny, Bézier and B-spline techniques, Springer Verlag, 2002.
[9] K. Karčiauskas, J. Peters, Guided spline surfaces, Computer Aided Geometric Design 26 (1) (2009) 105 – 116.
[10] J. Stam, Exact evaluation of Catmull-Clark subdivision surfaces at arbitrary parameter values, in: Proceedings of the ACM Conference on Computer Graphics (SIGGRAPH-98), ACM Press, New York, 1998, pp. 395–404.
[11] D. Doo, M. Sabin, Behaviour of recursive division surfaces near extraordinary points, Computer-Aided Design 10 (1978) 356–360.
[12] J. Peters, U. Reif, Subdivision Surfaces, Vol. 3 of Geometry and Computing, Springer-Verlag, New York, 2008.
[13] K. Karčiauskas, J. Peters, Curvature continuous bi-4 constructions for scaffold- and sphere-like surfaces, Computer Aided Design (SPM 2016) 78 (2016) 48–59.
[14] K. Karčiauskas, J. Peters, Quad-net obstacle course, `http://www.cise.ufl.edu/research/SurfLab/shape_gallery.shtml`, accessed: 2018-1-18.

Appendix: The transition guide

Here a bi-5 guide $\mathbf{g}_5$ is constructed analogous to $\mathbf{g}$ but for $\mathbf{h} := \mathbf{t}_{CC}$. Correspondingly, we enlist a C^1 map $\mathbf{b}_5^{\triangle}$ of total degree 5 with the same structure as $\mathbf{b}^{\triangle}$, see Fig. 30a. We use the same notation for groups of BB-coefficients with one key difference: to better capture second-order data, both $\mathbf{b}_|$, $\mathbf{h}_|$ and $\mathbf{t}_|$ now consist of 6 BB-coefficients per sector boundary (see black bullets in Fig. 30a and green bullets in Fig. 30c).

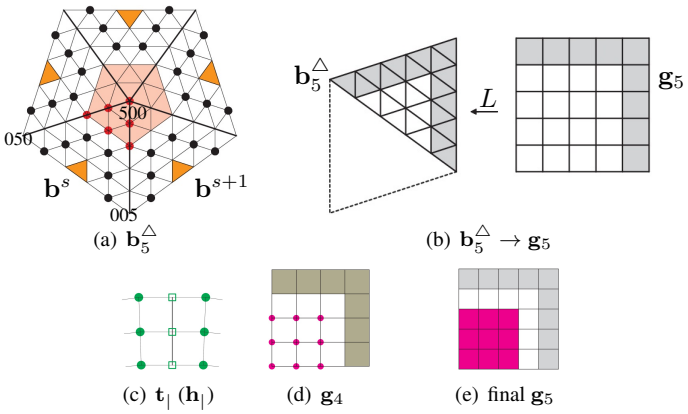

(a) $\mathbf{b}_5^{\triangle}$ (b) $\mathbf{b}_5^{\triangle} \to \mathbf{g}_5$ (c) $\mathbf{t}_|$ ($\mathbf{h}_|$) (d) $\mathbf{g}_4$ (e) final $\mathbf{g}_5$

Figure 30: (a) A piecewise C^1 map of total degree $d = 5$. (b) Increasing the flexibility via linear shear L. (c) $\mathbf{h}_|$ of $\mathbf{h}$. (d) Switching to auxiliary bi-4 map $\mathbf{g}_4$. (e) Final G^1 bi-5 guide $\mathbf{g}_5$.

The construction mimics the process in Section 3 and is done once to generate a linear map that is tabulated.

- Initialize $\mathbf{g}_5 := \mathbf{b}_5^{\triangle} \circ L$.
- Compose the tensor-border $\mathbf{t}$ from three corner jets $[\mathbf{g}_5 \circ \tilde{\chi}^{\square}]_{3\times 3}^4$.
- Choose $\mathbf{b}_|$ so that all 6 BB-coefficients of $\mathbf{t}_|$ (cyan bullets in Fig. 10 straddling the sector boundary) match the corresponding BB-coefficients of $\mathbf{h}_|$, see Fig. 30c.
- For each sector, $[\mathbf{g}_5^s]_{3\times 3}^4$ are assembled as in Fig. 3c to create an auxiliary map $\mathbf{g}_4$ (Fig. 30d; the khaki underlay indicates that $\mathbf{g}_4$ is only C^0).
- The 9 magenta bullets of each sector of $\mathbf{g}_4$ (Fig. 30d) are defined so that the 9 BB-coefficients of $\mathbf{t}$ sampled from $\mathbf{g}_4$ and with indices $i, j \in \{0, 1, 2\}$ (magenta in Fig. 10b) coincide with the corresponding 9 BB-coefficients of $\mathbf{h}$.
- Each sector of $\mathbf{g}_4$ is degree-raised to bi-5 to define 16 magenta underlaid BB-coefficients of $\mathbf{g}_5$.
- The central point is set by (7) (by (8) for $n = 3$).
- The remaining 5 degrees of freedom are set by (9).